

Machine-learned, finite temperature Fermi-operator expansions suitable for GPUs and AI-hardware

Stanislaw Kowalski,^{1,2, a)} Christian F. A. Negre,¹ Anders M. N. Niklasson,¹ Kipton Barros,^{1, b)} and Joshua Finkelstein^{1, c)}

¹⁾ *Theoretical Division, Los Alamos National Laboratory*

²⁾ *Daniel Guggenheim School of Aerospace Engineering, Georgia Institute of Technology*

(Dated: 12 May 2026)

We present several finite-temperature recursive Fermi-operator expansion schemes based on the second-order spectral projection (SP2) method. Our approach builds on a previous observation that the electronic structure problem, as formulated through a recursive SP2 expansion, can be mapped onto the architecture of a deep neural network. Using this perspective, we generalize SP2 to finite electronic temperatures and construct machine learning models to determine optimized expansion coefficients. These coefficients are trained for a specified chemical potential and electronic temperature and are not available in closed analytical form. However, by employing an appropriate affine rescaling strategy to the Hamiltonian matrix, we eliminate the need to retrain the model during a simulation if the temperature and chemical potential change. Our approach avoids explicit diagonalization and relies solely on highly optimized matrix-matrix multiplication kernels. Compared to state-of-the-art diagonalization, we achieve an order-of-magnitude speedup in the single-particle finite-temperature density matrix calculation for small and moderately sized matrices on modern GPUs and dense matrix multiply units.

I. INTRODUCTION

Quantum mechanics and electronic structure theory provide a complete theoretical framework for describing phenomena relevant to materials science, chemistry, and biology. In practical applications, however, the computational complexity prohibits the exact many-body solution to the Schrödinger equation. As a result, a variety of approximate electronic structure methods have been developed, balancing various levels of theory with computational cost. Among these, the most widely used methods are based on the Kohn-Sham density functional theory (KS-DFT),¹⁻⁴ within the Born-Oppenheimer approximation.⁵

In these approaches, the computational cost is governed by an algebraic eigenvalue problem. Solving the eigenvalue problem through diagonalization exhibits a computational cost that scales cubically with system size,⁶ which for systems beyond a few thousand atoms typically becomes prohibitively expensive. Consequently, alternative techniques, such as numerically thresholded sparse matrix algebra⁷⁻⁹ or various divide-and-conquer-like approaches,¹⁰⁻¹³ have been developed. Some of the most efficient methods are based on recursive Fermi-operator expansion schemes, in which the effective single-particle density matrix is computed directly, rather than constructed from the individual eigenvectors and eigenvalues.¹⁴⁻²³

Unfortunately, the most efficient recursive Fermi-operator expansion schemes are restricted to zero elec-

tronic temperature, which results in an idempotent density matrix. These recursive schemes therefore cannot model systems with fractional orbital occupations, which are often needed to capture, for example, degenerate eigenstates at the chemical potential for chemical reactions or systems at elevated electronic temperatures. The purpose of this work is to demonstrate how a zero-temperature recursive expansion scheme can be generalized to enable the computation of the Fermi-operator for systems with fractional occupation numbers, using extremely accurate polynomial approximations to the true Fermi distribution function.

An earlier attempt to construct a reasonably accurate pseudo-recursive Fermi-operator expansion was based on a modification of the second-order spectral projection (SP2) method.¹⁷ In this approach, the SP2 recursion is deliberately truncated after a finite number of iterations to introduce an effective thermal smearing,²⁴ with higher electronic temperatures corresponding to earlier truncation. However, this truncated expansion remains inherently approximate and fails to reproduce key features of the exact Fermi function, particularly in the vicinity of the chemical potential where accuracy is often most critical. Notably, the exact Fermi distribution is only recovered in the limit of zero electronic temperature, indicating that an alternative formulation is required for finite-temperature applications.

Several alternative approaches for computing the finite-temperature density matrix without explicit diagonalization have been proposed, including Chebyshev expansions²⁵ and Padé approximants,¹⁸ though each presents its own limitations. At low temperatures, Chebyshev expansions typically require very high polynomial orders to suppress Gibbs oscillations. While the introduction of smoothing kernels²⁶ can mitigate these oscillations, the resulting approximation still deviates

^{a)}Electronic mail: skowalski@lanl.gov

^{b)}Electronic mail: kbarros@lanl.gov

^{c)}Electronic mail: jdf@lanl.gov

from the exact Fermi function near the chemical potential. For small but finite temperatures, accurately resolving all states may require hundreds or even thousands of Chebyshev terms, with each term requiring a corresponding matrix multiplication. Although reduced-scaling techniques—where the number of matrix multiplications grows instead with the square root of the polynomial order—have been developed,^{27–29} they may still fall short of practical efficiency and can exhibit ill-conditioning effects at large enough polynomial order.

Recursive Padé expansions avoid Gibbs oscillations and typically require only a small number of recursion steps, largely independent of temperature. Each recursion, however, requires the solution of a linear system, usually carried out with a few (1–4) conjugate gradient iterations,¹⁸ and while the number of recursions remains modest, the need to repeatedly perform linear solves is computationally burdensome. Both Chebyshev- and Padé-based Fermi-operator expansions therefore incur a significant cost through the potentially large number of matrix multiplications or repeated linear solves. In practice, this overhead can outweigh their benefit, making them less efficient than direct diagonalization—particularly on modern GPU architectures, where highly optimized vendor-supplied routines achieve exceptional performance.

Previous work has demonstrated highly-performant implementations of SP2 using GPUs^{30,31} and, more recently, AI-oriented hardware such as NVIDIA Tensor Cores,^{32,33} enabling evaluation of the zero-temperature density matrix in significantly less time than the optimized Nvidia cuSOLVER diagonalization routines across a wide range of matrix sizes. Beyond these performance gains, this previous work highlighted that the recursive algebraic structure of SP2 maps naturally onto the architecture of a deep neural network, suggesting that its recursive second-order form could be systematically exploited with machine learning. This viewpoint provides new flexibility in constructing recursive expansions: rather than relying exclusively on analytically determined spectral projection (SP2) functions, we introduce polynomial functions with machine learned coefficients (or, weights) at each iteration to capture the exact Fermi function at arbitrary temperature. This idea, introduced in Ref. 32, forms the central focus of the present work and enables the reproduction of virtually exact Fermi functions at low computational cost for finite-temperature systems and cases with vanishing electronic HOMO–LUMO gaps.

We begin by presenting some general theoretical background for density functional theory and the SP2 method in Section II. In Section III we discuss our generalizations of SP2 to finite temperatures based on several different types of neural network architectures, details on how we train those models and how we can use them to efficiently compute the electronic entropy. In Section IV, we demonstrate and provide a workflow for how these schemes can be implemented and applied to construct

the finite-temperature density matrix. Lastly, in Section V we discuss our numerical results and computational performance using Nvidia Tensor Cores as well as how we can estimate model layer count.

II. BACKGROUND

A. The quantum mechanical eigenvalue equation in KS-DFT

In Kohn-Sham density functional theory the effective single-particle electronic states (or molecular orbitals),

$$\psi_i(\mathbf{r}) = \sum_j v_j^{(i)} \phi_j(\mathbf{r}), \quad (1)$$

for a local basis-set $\{\phi_j\}$, are obtained from the eigenvectors, $v^{(i)} = \{v_j^{(i)}\}$, of the Kohn-Sham Hamiltonian matrix,

$$H_{ij} = \langle \phi_i | \hat{H} | \phi_j \rangle = \int \phi_i^\dagger(\mathbf{r}) \hat{H} \phi_j(\mathbf{r}) d\mathbf{r}, \quad (2)$$

i.e. from the matrix eigenvalue equation,

$$Hv^{(i)} = \varepsilon_i v^{(i)}. \quad (3)$$

For simplicity, we assume the local basis-set representation, $\{\phi_j\}$, is orthonormal, i.e., where $\langle \phi_i | \phi_j \rangle = \delta_{ij}$, \hat{H} is the Kohn-Sham Hamiltonian operator and $\{\varepsilon_i\}$ are the Kohn-Sham eigenvalues. The electronic density is then given by

$$\rho(\mathbf{r}) = \sum_i f_i |\psi_i(\mathbf{r})|^2, \quad (4)$$

with occupation factors, f_i , which we can interpret as the probability of an electron residing in state ψ_i . Ground-state Kohn-Sham DFT is typically characterized by the eigenstates having integer occupation numbers, i.e. $f_i = 1$ for the occupied states and $f_i = 0$ for the unoccupied ones. This corresponds to f_i being represented by a Heaviside step function,

$$f_i = \Theta(\mu - \varepsilon_i), \quad (5)$$

where μ is the chemical potential, or Fermi level, chosen such that the total sum of the occupation numbers equals some given total number of states, $N_{\text{occ}} = \frac{1}{2} N_{\text{electrons}}$, i.e.

$$\sum_i f_i = N_{\text{occ}}. \quad (6)$$

However, in many cases, for example in metals, the electronic temperature is high in comparison to the electronic HOMO-LUMO gap, i.e. the difference in energies between the Highest Occupied Molecular Orbital and the

Lowest Unoccupied Molecular Orbital. In this case, fractional occupation numbers that are different from 0 and 1 are needed.

A solution is offered by extending ground-state KS-DFT to finite electronic temperatures,^{3,34} where the electronic structure is treated in terms of an ensemble using fractional occupation numbers where f_i are real numbers in the unit interval, i.e. $f_i \in [0, 1]$. For low lying states the occupation is close to 1 and for states at high energies the occupation numbers are close to 0. However, for intermediate states, with energies close to μ , which normally separates the fully occupied states from the unoccupied, the occupation number varies continuously between 1 and 0, and how fast it changes, depends on the temperature.

In finite temperature KS-DFT,³ the function that describes the fractional occupation number is the Fermi function

$$f_i = \left[e^{\beta(\varepsilon_i - \mu)} + 1 \right]^{-1}, \quad (7)$$

where $\beta = 1/(k_B T)$ is the inverse temperature and k_B is Boltzmann's constant. At elevated temperatures the step-like Fermi function becomes increasingly smeared, whereas in the low-temperature limit, i.e. when $\beta \rightarrow \infty$, the Fermi function in Eq. (7) becomes exactly the step function in Eq. (5).

Evaluating the Fermi function on the KS Hamiltonian matrix H gives the density matrix, D , where

$$D = \left[e^{\beta(H - \mu I)} + I \right]^{-1} \quad (8)$$

which completely describes the electronic structure of the physical system represented by H and from which the expectation of any observable A can be calculated

$$\langle A \rangle = \text{Tr}(DA). \quad (9)$$

Throughout the remainder of the text, we take f to denote the Fermi function

$$f(\varepsilon) = \frac{1}{1 + e^{\beta(\varepsilon - \mu)}}. \quad (10)$$

B. Second-order spectral projection (SP2)

Construction of an analytical quadratically convergent method for the zero-temperature step function can be derived intuitively by designing an approach that projects the higher eigenenergies of the Kohn-Sham Hamiltonian to 0 and the lower energies to 1 iteratively in order to achieve a desired occupation number, corresponding to a purified idempotent density matrix. The original SP2^{17,20,22} approach starts with a linear transformation, X_0 , of the Hamiltonian matrix H , where the spectrum of H is mapped to the interval $[0, 1]$ in reverse order. Iterative updates, $X_{i+1} = F(X_i)$, are then applied with

second-order matrix polynomials that bring the eigenvalues closer to either 0 or 1, sometimes referred to as *purification*. A squaring operation, $F(X) = X^2$, reduces all eigenvalues towards 0, and a similar attractor can be constructed around 1 with $F(X) = I - (I - X)^2 = 2X - X^2$, which brings eigenvalues closer to 1. At the same time, this process raises or lowers the total trace of the system, which can be used to successively approach the desired occupation number. The SP2 scheme is therefore sometimes also referred to as a trace-correcting scheme.

We now describe the SP2 method precisely. Given a Hamiltonian matrix, H , and spectral bounds $\varepsilon_{\min} \leq \lambda_H \leq \varepsilon_{\max}$, H is first transformed so that its spectrum is flipped and lies inside the unit interval $[0, 1]$

$$H' \equiv \frac{1}{\varepsilon_{\max} - \varepsilon_{\min}} (\varepsilon_{\max} I - H), \quad (11)$$

with I being the identity matrix. Setting $X_0 = H'$, an SP2 projection is then given by

$$X_{i+1} = \begin{cases} X_i^2 & \text{if } |\text{Tr}(X_i^2) - N_{\text{occ}}| \\ & < |\text{Tr}(2X_i - X_i^2) - N_{\text{occ}}| \\ 2X_i - X_i^2 & \text{otherwise} \end{cases} \quad (12)$$

with the algorithm terminating once $|\text{Tr}(X_{i+1}) - N_{\text{occ}}|$ is sufficiently small or depending on the available numerical accuracy.³⁵ In other words, the polynomial chosen in each iteration, either X^2 or $2X - X^2$, is here chosen to be the one that brings the trace of the applied matrix polynomial closest to N_{occ} . Other choices are possible, including pre-determined sequences of the spectral projections. For example, if the chemical potential μ is known instead of the occupation, Eq. (12) can be adapted. A similar update rule can be used with the updates of μ to determine which polynomial is chosen instead of a trace condition. Putting

$$\mu_0 = \mu' = \frac{1}{\varepsilon_{\max} - \varepsilon_{\min}} (\varepsilon_{\max} - \mu), \quad (13)$$

and again,

$$X_0 = H' \equiv \frac{1}{\varepsilon_{\max} - \varepsilon_{\min}} (\varepsilon_{\max} I - H), \quad (14)$$

iteration $i + 1$ of SP2 for a known chemical potential μ and unknown occupation is

$$X_{i+1} = \begin{cases} X_i^2 & \text{if } |\mu_i^2 - \mu'| \\ & < |2\mu_i - \mu_i^2 - \mu'| \\ 2X_i - X_i^2 & \text{otherwise} \end{cases} \quad (15)$$

where the updates to μ' are tracked and μ_{i+1} is chosen such that

$$\mu_{i+1} = \begin{cases} \mu_i^2 & \text{if } |\mu_i^2 - \mu'| \\ & < |2\mu_i - \mu_i^2 - \mu'| \\ 2\mu_i - \mu_i^2 & \text{otherwise} \end{cases} \quad (16)$$

Similarly to Eq. (12), the method can be terminated if $|\mu_{i+1} - \mu'|$ is small enough relative to a preselected tolerance. In other words, we choose the polynomial X^2 at iteration $i+1$ if μ_i^2 is closest to μ' and choose $2X - X^2$ otherwise. Interestingly, since $\mu' \in (0, 1)$ is essentially arbitrary, the procedure in Eq. (15) in fact shows how any real number in the unit interval can be approximated with a second-order recursive polynomial expansion. Crucially, the function applied (i.e. the precise sequence of either X_i^2 or $2X_i - X_i^2$) is now dependent strictly on the parameter μ , and entirely independent of the input X .

III. ALGORITHMS

The recursive SP2 Fermi-operator expansion scheme converges to a matrix step function of the Hamiltonian, with the step formed at the chemical potential. This corresponds to a matrix Fermi function at zero electronic temperature, $T = 0$, where the occupation numbers, f_i , are either 0 or 1. At elevated electronic temperatures this is no longer the case and the SP2 scheme is no longer valid. However, by re-interpreting and generalizing the SP2 scheme in terms of various deep neural network architectures, with flexible weights and bias coefficients, we can train or optimize these coefficients such that the different expansions approximate the Fermi functions with fractional occupation numbers at any chosen electronic temperature and chemical potential.

First we will discuss a deep neural network formulation of the SP2 scheme itself and then propose a set of extensions and generalizations of the SP2 scheme for finite temperature Fermi-operator expansion. We then apply the recursive approach also to the approximation of the electronic entropy function, which is needed to estimate the electronic free energy.

The method that we use for the training or optimization of the flexible expansion coefficients is presented afterwards. This optimization is a non-trivial task and requires an accurate initial guess. The initial guess is provided by the original SP2 scheme or its non-converged, truncated version, which resembles the shape of a Fermi function. For the approximation of the entropy function we can use a scaled polynomial of the Fermi function as an accurate initial guess.

A. Deep Spectral Refinement Networks

The recursive SP2 scheme in Eq. (12) looks very similar to the computational structure of a deep neural network (DNN), and this observation turns out to be quite powerful.³² In Ref. 32, the SP2 method described in Eq. (12) was expressed as a DNN using weights, W_i , biases, B_i , network layers, X_i , and a non-linear activation function, $h(X) = X^2$. Explicitly, the network parameters

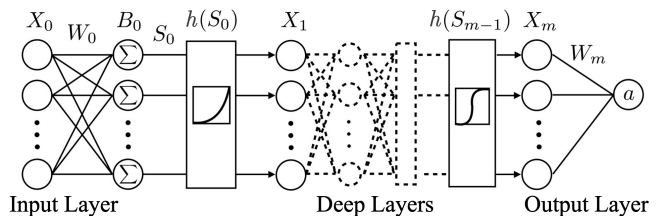


FIG. 1. Original description of DNN-SP2 in Ref. 32, showing weight W_i and bias B_i applied to the matrix X_i at each layer before squaring, which serves as the nonlinear activation function h . This form is equivalent to the MLSP2 method described in Eq. (24), without a running accumulator, and expresses the classic SP2 algorithm.

are

$$W_i = \sigma_i I \quad (17)$$

$$B_i = (1 - \sigma_i) S_{i-1} \quad (18)$$

where $\sigma_i = \pm 1$ is based on the trace of $S_i = W_i X_i + B_i$, and the $(i+1)$ -th network layer, X_{i+1} , is given by

$$X_{i+1} = h(S_i) = h(W_i X_i + B_i). \quad (19)$$

The matrix S_i , which is obtained from applying the weight and bias to the previous network layer, is the density matrix approximation at layer i . Notice that choosing $\sigma_i = 1$ leads to

$$S_i = 1S_{i-1}^2 + (1 - 1)S_{i-1} = S_{i-1}^2, \quad (20)$$

and choosing $\sigma_i = -1$ gives

$$S_i = -1S_{i-1}^2 + (1 + 1)S_{i-1} = 2S_{i-1} - S_{i-1}^2, \quad (21)$$

which is equivalent to the application of the polynomials X^2 and $2X - X^2$ in Eq. (12) at the i -th step. We call this DNN formulation of SP2, DNN-SP2.³² The neural network structure of DNN-SP2 is schematically shown in Fig. 1. We present this form for consistency with the literature, although it is not strictly necessary for B_i to be dependent in any way on S_{i-1} to ensure consistency with Eq. (12), and a form with constant weights and biases is presented in Sec III.

Notably, our input and nonlinearity have more structure than a usual neural network. Although the input is part of a vector space, it has the additional structure of a matrix, which is preserved by the linear layers and, crucially, the nonlinear activation function, both of which preserve the eigenspaces of the matrix, and act only on the eigenvalues (doing so by multiplication, without needing to calculate an eigendecomposition). In this sense, the network can be described as a scalar function (and indeed the machine-learned coefficients are trained on scalar inputs) applied as an analytic function on a matrix. This is easy to analyze in this instance because the matrices under consideration are Hermitian (or symmetric). There are multiple ways to consider this approach

beyond the original SP2 spectral projection or purification perspective, for example, as a form of generalized curve-fitting to analytic functions (with a recursive expansion as an alternative to more traditional expansions using orthogonal polynomials), or as a deep neural operator that can be trained to predict desired results.³² We find both viewpoints contribute significantly to our ultimate analysis and results, a detailed description of which, including a comparison to state of the art architectures such as ENNs, can be found in Appendix B.

1. Quadratic Layers with Accumulation (MLSP2)

In the same way that SP2 operates on the spectrum of a matrix, our machine learning models are one-dimensional and therefore trained on real values x inside the unit interval $[0,1]$. The simplest direct generalization of SP2, which here we call MLSP2 or SP2 with Learned Weights, features two stored values, one initialized as the input and quadratically dependent on each previous layer, and the other is an accumulator whose final value is the output of the network, allowing for slightly more expressibility than the original SP2 scheme. The update rule for MLSP2 method is written as

$$\begin{aligned} x_{i+1} &= \theta_{i,3} + \theta_{i,2} x_i + \theta_{i,1} x_i^2 \\ A_{i+1} &= A_i + \theta_{i,4} x_i \end{aligned} \quad (22)$$

for layer $0 \leq i < n$ and after n layers has output

$$A_n + x_n, \quad (23)$$

the approximation to the Fermi function f . The zeroth layer, x_0 , implements the spectrum flip as in Eq. (11), that is $x_0 = 1 - x$.

The accumulator, A_i , is a memory- and arithmetically-efficient way to provide more flexibility (and tunability) of the final output with respect to each layer in a manner that is not wholly dependent on the non-linear interaction with all subsequent layers, smoothing the loss landscape³⁶ and improving accuracy. Pseudocode for MLSP2 on the unit interval as presented in Eq. (22) is shown in Alg. 1.

Algorithm 1: MLSP2 approximating f at
 $x \in [0, 1]$

```

 $x = 1 - x$  ;
 $A = 0$  ;
for  $0 \leq i \leq n - 1$  do
     $a, b, c, d = \theta_{i,1}, \theta_{i,2}, \theta_{i,3}, \theta_{i,4}$  ;
     $A = A + d x$  ;
     $x = ax^2 + bx + c$  ;
end
 $f = A + x$  ;

```

Eq. (22) can naively be thought of as having $4n$ parameters, but strictly speaking this model has $2n + 2$ degrees

of freedom, as it can be re-expressed in a DNN-SP2-like form,

$$\begin{aligned} x_{i+1} &= (\theta_{i,1} + x_i)^2 \\ A_{i+1} &= A_i + \theta_{i,2} x_i \end{aligned} \quad (24)$$

with final output after n layers given by

$$A_n + \theta_{n,1} + \theta_{n,2} x_n. \quad (25)$$

Here, the weights $\{\theta\}$ need to be adjusted from Eq. (22) and the equivalency between these two forms is shown in Appendix C. This formulation may be more optimal on some architectures from an implementation perspective since it requires two fewer summations in each iteration.

Without the accumulator, Eq. (22) actually reduces to traditional SP2 when $\theta_{i,1} = \sigma_i$, $\theta_{i,2} = (1 - \sigma_i)$ and $\theta_{i,3} = 0$. The method shown in Eq. (22) is however capable of approximating much more than just a step function and can be fit to the exact thermal smearing of the Fermi function at any given temperature, instead of being truncated and scaled at some optimal number of layers as in Ref. 24. In Fig. 2 we show a comparison of this truncated SP2 algorithm from Ref. 24 for $\beta' = 308.3$ and $\mu' = 1/2$ with 20 layers, the number of layers necessary to match the derivative at the Fermi level as given by Eq. (66), and an MLSP2 model trained using Alg. 1. Even though the approximations to f look similar, a closer look at the error demonstrates the superior accuracy of MLSP2 in the fractional occupation numbers around the chemical potential. Discussion of the training procedure is given in Section III C.

2. Maximally Expressive Quadratic (Max-SP2)

We can generalize Eq. (24) or Eq. (19) by allowing a contribution from not only the previous layer and a constant bias, but also every previous layer. We call this scheme Max-SP2. Every layer is the square of a linear combination of all previous layers, which introduces the idea of “skip connections” from machine learning.³⁷ We again include a zeroth layer initialized as $1 - x$ which imitates the SP2 spectrum flip. The update rule for layer $0 \leq i < n$ is

$$\begin{aligned} x_{i+1} &= \left(\delta_i + \sum_{j=0}^i \theta_{i,j} x_j \right)^2 \\ A_{i+1} &= A_i + \gamma_i x_i \end{aligned} \quad (26)$$

and the output at layer $n + 1$ of

$$A_n + \gamma_n x_n, \quad (27)$$

yields the MaxSP2 approximation to f . Here the θ 's, γ 's and δ 's are trainable parameters scaling the various layer connections and the accumulation into the final output. The parameter $\gamma_n = \pm 1$ is determined by whether, in

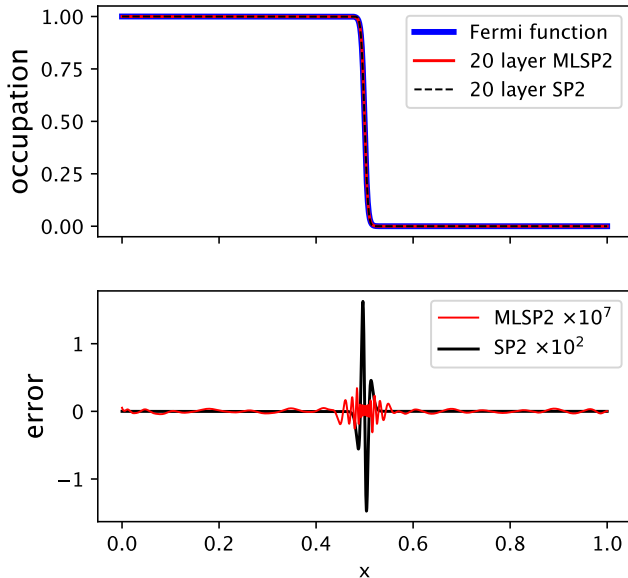


FIG. 2. (top) Comparison of a scaled and truncated SP2 approximation of the Fermi function as described in Ref. 24 with $\beta' = 308.3$ and $\mu' = 1/2$ with 20 layers and a trained MLSP2 model from Eq. (22). (bottom) Here we show the error measured pointwise between each approximation with the true Fermi function f . The SP2 error is on the order 10^{-2} , and the MLSP2 error is on the order of 10^{-7} , so they are magnified by those respective factors to make error more visible.

the SP2 initialization, $x_n = x_{n-1}^2$ or $x_n = 2x_{n-1} - x_{n-1}^2$, respectively. Analytically, it would seem all γ_i are redundant up to sign, as scalar magnitude can be transferred to the δ_i and $\theta_{i,j}$ terms, but it is initialized as 0 when starting from the SP2 scheme, so it must be kept as an additional parameter for the sake of numerical stability.

The approach in Eq. (26) is quite flexible and reaches higher accuracy with far fewer layers than the previous two, having $\mathcal{O}(n^2)$ parameters to tune, but requires memory scaling linearly in the layer count. This is the maximally expressive network architecture that uses a squaring as its nonlinear activation function, and provides a much larger number of parameters (per multiplication) to tune at the cost of additional matrix additions. Section V explores this tradeoff, and empirically finds it largely in favor of MLSP2 at high β in FP32 arithmetic, although this architecture could be necessary for FP64.

For the sake of completeness, we mention that an even more expressive alternative to Eq. (26) is possible if the squaring operation can be replaced by general matrix multiplication:

$$x_{i+1} = \left(\delta_i + \sum_{j=0}^i \phi_{i,j} x_j \right) \left(\delta'_i + \sum_{j=0}^i \psi_{i,j} x_j \right) \quad (28)$$

$$A_{i+1} = A_i + \gamma_i x_i$$

Relative to Eq. (26), this version nearly doubles the pa-

Algorithm 2: MaxSP2 approximating f on $[0,1]$

```

 $x_0 = 1 - x$ ;
for  $0 \leq i \leq n - 1$  do
   $x_{i+1} = \delta_i$ ;
  for  $0 \leq j \leq i$  do
     $x_{i+1} = x_{i+1} + \theta_{i,j} x_j$ ;
  end
   $x_{i+1} = (x_{i+1})^2$ ;
end
 $f = \gamma_0$ ;
for  $1 \leq i \leq n$  do
   $f = f + \gamma_i x_i$ ;
end

```

rameter count per layer, which may be advantageous at low β . We refer to this architecture as ArbitrarySP2 (ArbSP2), but it is not further explored in this work.

3. Recombinant Layers and Accumulators (Skip-SP2)

We can construct a “compressed” form of MaxSP2, which we call Skip-SP2, by generalizing Eq. (26), but with a finite memory. This method further leverages the idea of skip connections where now each layer i is the square (or activation function) of a linear combination of the k most recent layers, as well as K running accumulators and a constant offset $\alpha_{n,k}$:

$$x_{i+1} = \left(\alpha_{i,k} + \sum_{j=0}^{k-1} \alpha_{i,j} x_{i-j} + \sum_{j=1}^K \beta_{i,j} A_{i,j} \right)^2 \quad (29)$$

$$A_{i+1,j} = A_{i,j} + \gamma_{i,j} x_i$$

where k is number of layers stored, K is the number of accumulators, and α, β, γ are trainable coefficients of the linear recombination of the skip connections, accumulators contributing to x_i , and x_i contributing to the accumulators.

This captures the full expressibility of quadratics; any MLSP2 scheme can be embedded in Skip-SP2, but Skip-SP2 only has $(1 + k + 2K)n + 2$ parameters, allowing deeper fine-tuning while keeping memory constant in layer count n . Just one skip connection, $k = 1$, allows for qualitatively different behavior such as fusing two layers into an arbitrary 4th-order polynomial. Even not accounting for potential emergent behavior, this enables, for example, initialization with a 4th order spectral projection as found in Ref. 17.

B. Approximate Entropy Function

The electronic free energy, $g(x)$, is another important quantity which we may wish to calculate in addition to the density of states as it serves as a constant of motion in molecular dynamics. At finite electronic temperatures,

fractional occupation numbers appear in the free energy, defined as

$$g(x) = f(x)(x - \mu) - \beta^{-1}s(x), \quad (30)$$

for all real numbers x , and where $s(x)$ is the entropy function

$$s(x) = -f(x) \ln f(x) - (1 - f(x)) \ln(1 - f(x)). \quad (31)$$

Computing Eq. (30) is fairly straightforward if $f(x)$ and $s(x)$ are already known, but computing s as a function of f itself

$$s(f) = -f \ln f - (1 - f) \ln(1 - f), \quad (32)$$

is challenging as this involves calculating matrix logarithms.

Previous approaches to approximate the electronic entropy have used either a variationally-exact entropy computed by integrating the inverse of the SP2 scheme on the eigenvalues closest to the Fermi level (estimated via Lanczos method)²⁴ or polynomial expansions of the fractional occupation numbers or the density matrix directly.³⁸ The former case cannot be used here, as MLSP2 is not formally one-to-one on the region $[0, 1]$, and each iteration does not have a single defined inverse on that interval, over which integration would need be performed for the variationally correct entropy. In the latter case of a polynomial expansion in fractional occupation, s was approximated via

$$s \approx \sum_{i=1}^m c_i^{(m)} f^i (1 - f)^i, \quad (33)$$

where the coefficients, $\{c_i^{(m)}\}$, for various expansion orders m are given in Ref. 38, though the coefficients with even order in i have a sign error and should have opposite sign. The accuracy is good only around the chemical potential at $f = 0.5$ and quite poor towards the end points, although exact at $f = 0$ and $f = 1$. Unfortunately, this will always be the case for any polynomial expansion of s in f , as it has unbounded derivatives at $f = 0$ and $f = 1$ due to the logarithms. To get around this, we therefore need to expand in energy, x . We can start with Eq. (33) as an initial expansion, but we can now manipulate x before f is applied to it, and we can later allow replace f with a machine-learned approximation that makes our approximation to s nearly exact. If we begin with the $m = 1$ approximation with an altered function \tilde{y} instead of f ,

$$\tilde{s}(x) = (4 \ln 2) \tilde{y}(x)(1 - \tilde{y}(x)), \quad (34)$$

we are able to do even better than even the higher-order expansions in f by modifying the above $m = 1$ expansion and requiring that in addition to the matching behavior at certain points, second derivatives match as well.

Comparing the second derivatives of Eq. (31) and Eq. (34) at μ ,

$$s''(\mu) = -4(f'(\mu))^2 \quad (35)$$

$$\tilde{s}''(\mu) = -(8 \ln 2)(\tilde{y}'(\mu))^2, \quad (36)$$

and we see that we need

$$\tilde{y}'(\mu) = \frac{1}{\sqrt{2 \ln 2}} f'(\mu), \quad (37)$$

which we can accomplish with a recursive expansion for \tilde{y} by initializing it with a rescaling of our previous model (e.g. MLSP2),

$$\tilde{y}(x) = \tilde{f}(\alpha(x - \mu) + \mu), \quad (38)$$

with $\alpha = (2 \ln 2)^{-1/2}$. A model for learning the entropy function, based on for example Eq. (22), is then given by:

$$\begin{aligned} x_0 &= \alpha(x - \mu) + \mu \\ x_{i+1} &= \theta_{i,1} x_i^2 + \theta_{i,2} x_i + \theta_{i,3} \\ A_{i+1} &= A_i + \theta_{i,4} x_i \\ s_{n+1} &= (4 \ln 2) A_{n+1} (1 - A_{n+1}) \quad (\text{final layer}) \end{aligned} \quad (39)$$

where the familiar spectrum flip on x_0 is unnecessary due to the symmetry of s and \tilde{s} about μ , and $|\alpha| < 1$ guarantees x_0 falls within the range of validity of \tilde{f} provided β, μ do.

This approach preserves the properties of Eq. (34), since the linear transformation on the input preserves μ by construction and preserves values in the limit of $\pm\infty$ because $\alpha > 0$, while matching the second derivative at the critical point. This leads to an excellent initial guess. The recursive expansion for $s(x)$ in the form Eq. (39) can then be trained in the same manner as MLSP2 is trained to approximate $f(x)$, and with a similar final precision. The initialization of \tilde{y} with an already learned Fermi-operator expansion is the key in both bringing down the overall cost of training \tilde{s} and simply achieving convergence in the case of high β' . We observe an order-of-magnitude decrease in training time by initializing \tilde{y} with MLSP2 instead of SP2 and enabling rescaling on the $m = 1$ ansatz, making the learning of s via a recursive quadratic expansion substantially less costly.

The visual intuition for Eq. (34) can be seen in the first panel of Fig. (3) as the product of a ‘‘step-down’’ function, $f(x)$, with a ‘‘step-up’’ function, $1 - f(x)$, resulting in a Gaussian-like function visually similar to $s(x)$. The second panel then shows rescaling this resultant product vertically to match the peak of $s(x)$, and then horizontally to match the curvature of $s(x)$ at that peak. The third panel shows an error comparison between α set to the locally optimal value matching the second derivative, $\frac{1}{\sqrt{2 \ln 2}} \approx 0.849322$, and by least squares optimization over the interval, ~ 0.842704 , which gives an error around a tenth of a percent over the whole approximation.

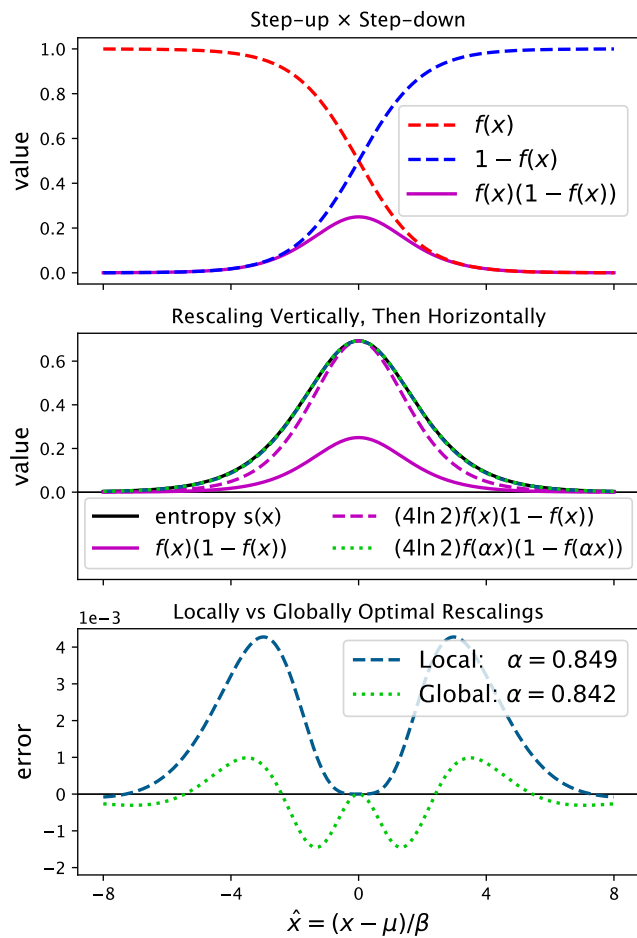


FIG. 3. A graphical process for creating approximations to $s(x)$ that serve as excellent weight initializations, which accelerates training dramatically. The 3rd panel displays the pointwise error of the two best approximations shown in the 2nd panel.

C. Training

1. Synthetic Data: Eigenvalue Sampling

As described up to now, networks can be trained using real numbers on $[0, 1]$ instead of on matrices with normalized spectra.

The method in which this scalar training data is sampled, however, has considerable impact on the accuracy of the model. Regularly or randomly sampling according to some weighting does not affect the training, but random re-sampling between training iterations (analogous to using stochastic gradient descent instead of gradient descent) stalls performance, preventing convergence below a certain threshold of error. Additionally, the weighting displays an interesting effect: if it is uniform, $p(x) \propto 1$, training acts to minimize the average error of the solution, while sampling incorporating the derivative of the Fermi function, $p(x) \propto 1 + |f'|$, or proportional to the

arc length,

$$\mu(x) \propto \sqrt{1 + (f')^2}, \quad (40)$$

acts to minimize the maximum error of the solution. At high values of β , it is necessary to incorporate a much higher rate of sampling (as satisfied by incorporating the derivative) around the Fermi level μ , or else fine detail around it is missed and training error is not truly representative of the maximum error.

2. Levenberg–Marquardt with Geodesic Acceleration

The optimizer plays a critical role in the success of our overall approach to learning model coefficients: the problem is highly sensitive and not capable of *exact* fits, but is nonetheless much closer to rootfinding than to traditional gradient descent. For such problems, the best optimizer is nonlinear least squares, i.e. Levenberg-Marquardt.³⁹

We initially trained these models with LsqFit.jl,⁴⁰ before moving to the more recent NonlinearSolve.jl.⁴¹ Numerical improvements between the two packages as well as the introduction of simple geodesic acceleration constitute the difference between taking a million iterations to plateau in accuracy versus taking only a few hundred, while achieving an even greater accuracy.

IV. WORKFLOW

Here we present a practical workflow for the algorithms developed in the previous sections and show how a single set of optimized Fermi-operator expansion coefficients can be used with expansions at various temperatures and fractional occupation. Our approach enables the training of a model at pre-selected β_0 and μ_0 to then be used within an entire region of normalized parameter space which makes the methodology practical for simulations where β or μ may change.

1. Affine Rescaling to Avoid Retraining

Although we are able to train a model at any given (β, μ) , we cannot do this for all possible (β, μ) pairs, and do not want to constantly re-fit the model through the course of a simulation or when a new condition is needed. Fortunately, the Fermi operator has the extremely convenient property that β and μ only affect the input up to an affine transformation of H . We leverage this by building a single model trained for parameters β_0, μ_0 , that is capable of representing an entire region of normalized (β', μ') parameter space with high accuracy. This region is called the region of validity.

Given a true H , β and μ , the normalized parameters

are

$$H' \equiv \frac{\varepsilon_{\max} I - H}{\varepsilon_{\max} - \varepsilon_{\min}} \quad (41)$$

$$\mu' \equiv \frac{\varepsilon_{\max} - \mu}{\varepsilon_{\max} - \varepsilon_{\min}} \quad (42)$$

$$\beta' \equiv (\varepsilon_{\max} - \varepsilon_{\min}) \beta \quad (43)$$

which ensure that

$$\begin{aligned} & (H - \mu I) \beta \\ &= \frac{H - \mu I}{\varepsilon_{\max} - \varepsilon_{\min}} (\varepsilon_{\max} - \varepsilon_{\min}) \beta \\ &= \frac{H - \varepsilon_{\max} I - \mu I + \varepsilon_{\max} I}{\varepsilon_{\max} - \varepsilon_{\min}} (\varepsilon_{\max} - \varepsilon_{\min}) \beta \\ &= \left(\frac{H - \varepsilon_{\max} I}{\varepsilon_{\max} - \varepsilon_{\min}} - \frac{\mu - \varepsilon_{\max}}{\varepsilon_{\max} - \varepsilon_{\min}} I \right) (\varepsilon_{\max} - \varepsilon_{\min}) \beta \\ &= (\mu' I - H') \beta'. \end{aligned} \quad (44)$$

In other words, H, β, μ and H', β', μ' generate the exact same density matrix, taking into account the spectrum flip used for the initial linear transformation of SP2. Similarly, if β_0, μ_0 are the parameters we train our model to, we can determine an H_0 such that H', β', μ' and H_0, β_0, μ_0 generate the same density matrix. Setting

$$(\mu_0 I - H_0) \beta_0 = (\mu' I - H') \beta', \quad (45)$$

leads to H_0 being given by

$$H_0 = \frac{\beta'}{\beta_0} (H' - \mu' I) + \mu_0 I. \quad (46)$$

The only condition we need impose is that the spectrum of H_0 lie inside $[0,1]$, a requirement of the models developed in Sec. III. But since this is already the case for H' by construction, this condition on H_0 leads to the inequality constraints

$$0 \leq \frac{\beta'}{\beta_0} (0 - \mu') + \mu_0 \quad \text{and} \quad \frac{\beta'}{\beta_0} (1 - \mu') + \mu_0 \leq 1, \quad (47)$$

or, equivalently,

$$\frac{\mu_0}{\mu'} \beta_0 \geq \beta' \quad \text{and} \quad \frac{1 - \mu_0}{1 - \mu'} \beta_0 \geq \beta'. \quad (48)$$

These non-linear constraints define the region of validity of (β', μ') parameter space, for which the trained model with Hamiltonian H_0 and parameters β_0, μ_0 , has the same density matrix as H', β', μ' , and thus of the original problem H, β and μ . The regions of validity for the example cases of $\beta_0 = 40, \mu_0 = 0.3$ and $\beta_0 = 1500, \mu_0 = 1/3$ are shown in Fig. 4.

The rescalings of temperature may require training β_0 for very high values in order to capture low electronic temperatures. The temperature scaling factor in Eq. (43) will depend on the spectral range of the underlying Hamiltonian and should be taken into account

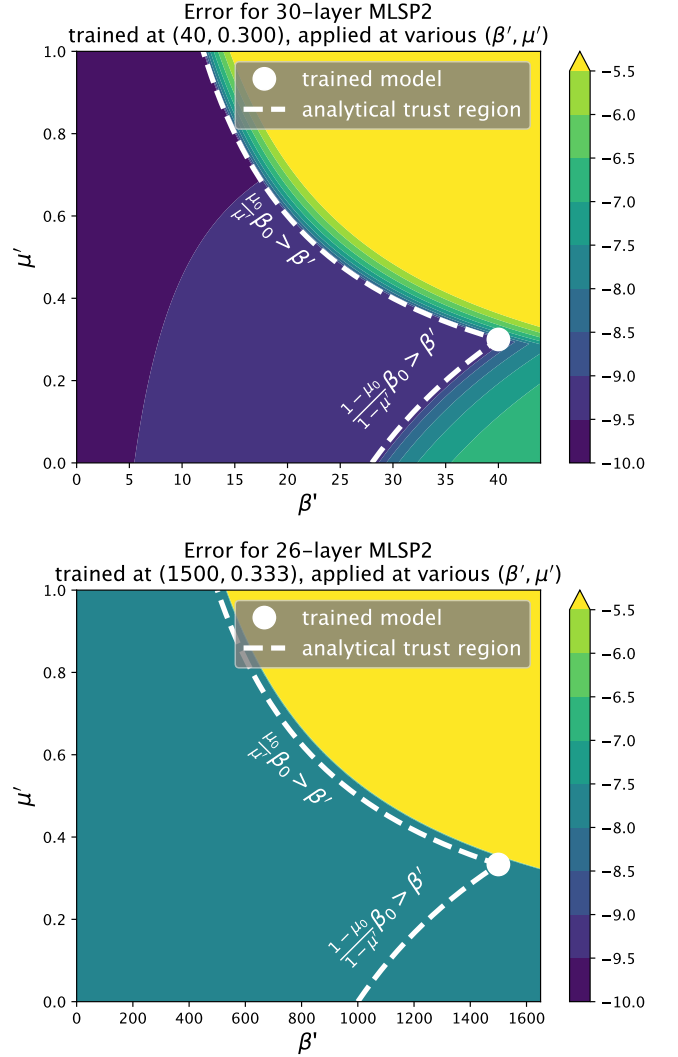


FIG. 4. (top) Error of a model trained at $\beta_0 = 40, \mu_0 = 0.3$ when applied to a region of β', μ' normalized parameter space. The region of validity is the (blue) area in the plane with error (in the max norm) less than 10^{-9} to the left of dashed lines indicated by Eq. (48). The negative exponent associated to each color, representing the model error, is shown on the right, with yellow regions having unbounded max error (at least $10^{-5.5}$). (bottom) Same plot but for $\beta_0 = 1500$ and $\mu_0 = 1/3$, with error allowed to go as high as $10^{-7.5}$ in the region of validity.

when training a model at the point (β_0, μ_0) . This idea is discussed further in Sec. VC where we provide an upper bound on the accurately representable β' values for a given β_0 . In Alg. 3 we display pseudocode which implements a calculation of the density matrix using the normalizations and rescalings discussed in this section. A fully working python implementation of MLSP2 trained for the $(\beta_0, \mu_0) = (1500, 1/3)$ model has also been included in Sec. A of the Appendix.

Just as the procedure discussed in this paper for training recursive quadratic expansions can be applied to any

Algorithm 3: Using MLSP2 with normalizations to compute D

Determine spectral bounds $\varepsilon_{\min}, \varepsilon_{\max}$;
 $\mu' = \frac{\varepsilon_{\max} - \mu}{\varepsilon_{\max} - \varepsilon_{\min}}$;
 $\beta' = (\varepsilon_{\max} - \varepsilon_{\min})\beta'$;
 $H' = \frac{-1}{\varepsilon_{\max} - \varepsilon_{\min}}H + \frac{\varepsilon_{\max}}{\varepsilon_{\max} - \varepsilon_{\min}}I$;
 $X = \frac{\beta'}{\beta_0}H' + \left(\mu_0 - \frac{\beta'}{\beta_0}\mu'\right)I$;
 $A = 0$;
for $1 \leq i \leq n$ **do**
 $a, b, c, d = \theta_{i,1}, \theta_{i,2}, \theta_{i,3}, \theta_{i,4}$;
 $A = A + dX$;
 $X = aX^2 + bX + cI$;
end
 $D = A + X$;

analytic function on a square matrix (so long as a good initial guess is provided), the procedure outlined in this section to reuse a model trained for a particular (β, μ) point can be generalized and used for any family of matrix functions where, like the Fermi function, the parameters only act in an affine manner on the input, or where an affine transformation on the input matrix results in a similar transformation on the output

$$P(aX + bI) = Q(a, b)P(X) + R(a, b)I, \quad (49)$$

where Q, R can be any arbitrary functions, since a and b are scalars. Many potentially significant families of functions fall into this category, such as exponentials, $e^{aX+bI} = e^{aX}e^{bI} = e^b e^{aX}$, or, with $b, R = 0$, square roots, $P(cX) = \sqrt{c}P(X)$, logarithms, $P(aX) = \ln(a)I + P(X)$, and orthogonalization,⁴² $P(cX) = P(X)$.

2. Determining Chemical Potentials Using the Newton–Raphson Method

In electronic structure calculations, we often know the total number of electrons in the system, N_{occ} , *a priori* but not the chemical potential, μ . Since the density matrix depends on μ it needs to be determined iteratively. To do so, we can solve the equation

$$g(\mu) \equiv N_{\text{occ}} - \text{Tr}(D) = 0, \quad (50)$$

using Newton–Raphson.⁴³ This requires a derivative of g , which in turn requires differentiating the density matrix with respect to μ . In Ref. 24, the approximation to D is inexact, and exactly evaluating the derivative via forward differentiation doubles the number of required matrix-matrix multiplications. The density matrix D satisfies the logistic differential equation in μ , since it is a logistic function of the Hamiltonian

$$\frac{\partial D}{\partial \mu} = -\beta D(I - D). \quad (51)$$

Therefore $g'(\mu)$ can be evaluated with no additional matrix multiplications since,

$$g'(\mu) = -\text{Tr}\left(\frac{\partial D}{\partial \mu}\right) = \beta \text{Tr}(D) - \beta \text{Tr}(D^2), \quad (52)$$

and

$$\text{Tr}(D) = \sum_{i=1}^N D_{ii} \quad (53)$$

$$\text{Tr}(D^2) = \sum_{i=1}^N \sum_{j=1}^N |D_{ij}|^2. \quad (54)$$

This approach was used only as an approximation in Ref. 24, but here it is exact. Thus the iterative correction to μ can be easily computed

$$\Delta\mu = -\frac{g(\mu)}{g'(\mu)} = -\frac{N_{\text{occ}} - \text{Tr}(D)}{\text{Tr}(\beta D(I - D))}. \quad (55)$$

Because Newton–Raphson is quadratically convergent, with a sufficiently close guess, only one iteration of this procedure may be necessary. However, it should be noted while this same procedure needs to be done for diagonalization-based methods, they incur the cost of diagonalization only once, at the decomposition of H , because Eqs. (50) and (55) can be evaluated and updated using purely the diagonal of the Hamiltonian.

3. Generalized SP2 Workflow

In this section we describe the step-by-step procedure for how to use any generalized MLSP2 method to compute the finite-temperature density matrix for a known occupation or chemical potential. Figure 5 condenses these steps into an easy-to-read flowchart. If μ is already known, there is no iterative update to μ and the outer loop in Fig. 5 is not needed.

1. Obtain a Hamiltonian H and electronic temperature β .
2. Furnish an initial guess for μ which is likely to be very close to the true solution.
3. Estimate the spectral bounds of H and rescale $(H, \beta, \mu) \rightarrow (H', \beta', \mu')$.
4. Pick the cheapest available model (β_0, μ_0) that contains (β', μ') within its bounds according to Eq. (48). H' is then rescaled according to Eq. (46) to yield H_0 .
5. The model (β_0, μ_0) is applied to H_0 to compute the finite-temperature density matrix D .
6. D is obtained and if necessary, $\text{Tr}(D)$ is checked against the desired occupation number N_{occ} .

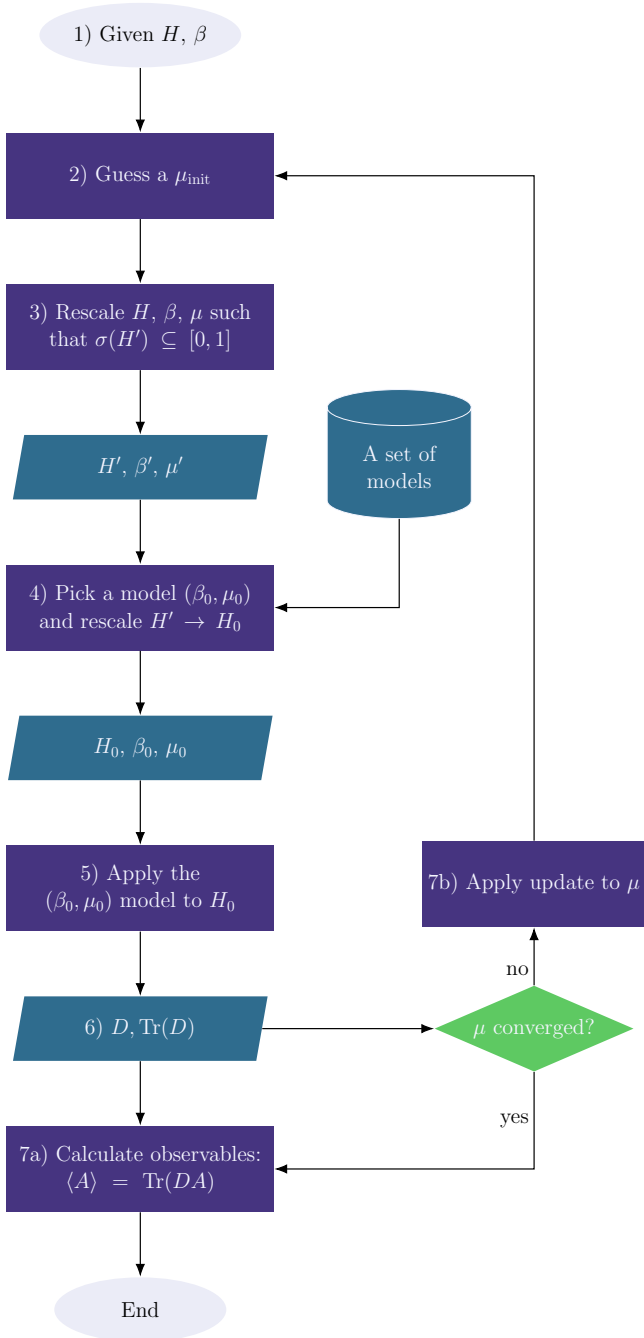


FIG. 5. This flowchart describes the process of applying the generalized MLSP2 algorithm to arbitrary Hamiltonians. Blocks demonstrate procedures, parallelograms contain intermediate data, the cylinder contains the database of available models, and the diamond represents the convergence criterion of some iterative method for the chemical potential.

7a. If these match sufficiently well, use D to compute quantum observables of interest according to Eq. (9).

7b. If they do not, we update μ (e.g. through a Newton-Raphson step) and re-evaluate D with a more pre-

cise μ .

If weights for multiple families of algorithms are stored, such as MLSP2, Skip-SP2, or MaxSP2, model selection (Step 4) can be done over each family, ultimately using one with the most favorable properties (such as minimum layer count subject to accuracy and memory constraints).

V. NUMERICS

A. Tensor Cores and mixed-precision

For a symmetric matrix, X represented in single-precision, the squaring operation $X \mapsto Y = X^2$ can be computed using mixed-precision arithmetic by decomposing X into two half-precision summands, X_0 and X_1 and then expanding the product using FP16 matrix multiplications with FP32 accumulations (which is denoted as FP16/FP32),³²

$$\begin{aligned}
 X_0 &= \text{FP16}[X] \\
 X_1 &= \text{FP16}[X - \text{FP32}[X_0]] \\
 Y_0 &= X_0 X_0 \\
 Y_1 &= X_0 X_1 \\
 Y &\approx Y_0 + Y_1 + Y_1^\top.
 \end{aligned} \tag{56}$$

We thus approximately obtain a square of an FP32 symmetric matrix using only two FP16/FP32 matrix-matrix multiplications. There is no equivalent trick for multiplying two non-symmetric X_0 and X_1 however, since in that case $Y_1^\top \neq X_1 X_0$, and three multiplications would be required.

Recently, Nvidia has integrated support for similar mixed-precision acceleration schemes into cuBLAS,⁴⁴ that emulates higher precision multiplications using integer or low precision floating point data types on Tensor Cores based on the Ozaki scheme.⁴⁵ This emulation preserves both range and accuracy, but requires many more multiplications than the two needed in Eq. (56). Our approach leverages the inherent symmetry of our matrices, the fact that we require only a squaring operation and discards terms smaller than 2^{-22} , the square of the FP16 unit round-off, which is both practically and rigorously justified.^{32,46}

An efficient approach to evaluating Eq. (22) via Eq. (56) on such hardware can be given by Alg. 4, where optimizations have been made for the sake of minimizing data transfer.

Since Tensor Cores can give FP32 output (as a result of accumulating in FP32) there is no need to re-typecast to higher precision. The first line after generating X_0, X_1 in Alg. 4 gives $aY_0 + bX$, which is symmetric, the next line gives $aY_1 + \frac{1}{2}(aY_0 + bX)$, and the addition thereafter gives:

$$\frac{1}{2}(aY_0 + bX) + \frac{1}{2}(aY_0^\top + bX^\top) + aY_1 + aY_1^\top \tag{57}$$

Algorithm 4: Mixed Precision MLSP2

```

a, b, c, d =  $\theta_{i,1}, \theta_{i,2}, \theta_{i,3}, \theta_{i,4}$  ;
A = A + d X ;
X0 = float_to_half(X) ;
X1 = float_to_half(X - X0) ;
X = aX0X0 + bX ;
X2 = X + X⊤ ;
X = X2 + cI ; // Xi+1 = aXi2 + bXi + cI

```

which, by symmetry again, reduces to:

$$a(Y_0 + Y_1 + Y_1^\top) + bX = aX^2 + bX. \quad (58)$$

This removes the need for one matrix addition kernel compared to the naive implementation of Eq. (56). Further, $A = A + dX$ can be neglected when d is less than some threshold, e.g. 10^{-8} , which is the case for about half of layers, and training can be done with $c = 0$ as the SP2 initialization has no constant term, replacing the last addition with a simple swap of pointers to X and $X2$.

All together, this reduction in data transfer improves efficiency from $\sim 73\%$ at large matrix sizes in the naive implementation to $\sim 90\%$, resulting in a gain of 30 Tflops on the RTX 6000 Ada.

B. Layer Count

The learned weights of MLSP2 empirically tend to be similar to the original SP2 coefficients. This helps us to derive a reasonable estimate for the number of layers, n_ℓ , required to train the MLSP2 model by looking at how large of a polynomial order is needed for the SP2-generated polynomial to approximate the true derivative of the Fermi function evaluated at μ' , $f'(\mu') = \beta'/4$. Intuitively, we need a steep enough polynomial in order to be able to match derivatives at the chemical potential.

Surprisingly, an estimate can be made as a natural consequence of the fact that the inverse of the golden ratio, $\varphi \approx 1.618$, is a fixed point of the composition of $f_0(x) = x^2$ with $f_1(x) = 2x - x^2$.

Setting $\phi = \varphi^{-1}$, it is simple to verify that $f_0(\phi) = \phi^2$, and that

$$f_1(\phi^2) = 2\phi^2 - \phi^4 \quad (59)$$

$$= \phi^2(2 - \phi^2) \quad (60)$$

$$= \phi^2(\underbrace{(\phi + 1)}_{=\phi^{-1}} - \underbrace{(\phi^2 + \phi - 1)}_{=0}) = \phi, \quad (61)$$

so that $(f_1 \circ f_0)(\phi) = \phi$. Note also that

$$f'_0(\phi) = 2\phi \quad (62)$$

$$f'_1(\phi^2) = 2(1 - \phi^2) = 2\phi.$$

If the initial linear transformation of SP2 in Eq. (15) maps μ to ϕ , an alternating sequence of f_0 and f_1 compositions

$$\tilde{f}_{n_\ell} \equiv f_{n_\ell \bmod 2} \circ \dots \circ f_1 \circ f_0 \quad (63)$$

MLSP2 & maxSP2 Accuracy vs Layer Count (FP64)

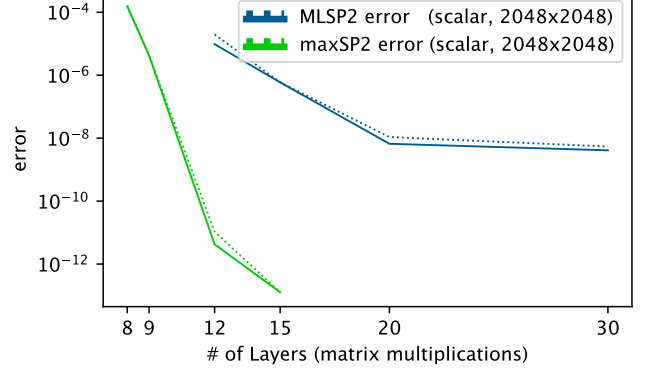


FIG. 6. Model accuracy versus layer count at $\beta = 40$, $\mu = 0.3$, showing the error as a function of number of layers. In this case we are not limited by polynomial order, but rather expressibility. By Eq. (66), $\beta = 40$ only requires 11 layers to match derivatives.

approximates the step function (proof shown in the Appendix)

$$\Theta_j(x) = \begin{cases} 0, & x < \phi \\ \phi^j, & x = \phi \\ 1, & x > \phi \end{cases}, \quad (64)$$

on $[0, 1]$ with $j = 1$ if n_ℓ is odd, and $j = 2$ if n_ℓ is even. By the chain rule and induction, the derivative of \tilde{f}_{n_ℓ} at ϕ is then

$$\begin{aligned} \tilde{f}'_{n_\ell}(\phi) &= f'_{n_\ell \bmod 2}(\phi^j) \frac{d}{dx} (f_{n_\ell - 1 \bmod 2} \circ \dots \circ f_0)(\phi) \\ &= (2\phi)^{n_\ell}, \end{aligned} \quad (65)$$

Thus setting \tilde{f}'_{n_ℓ} equal to the derivative of the Fermi function at $\mu' = \phi$ yields an estimate for n_ℓ of

$$n_\ell = \frac{\ln(\beta'/4)}{\ln(2\phi^{-1})} \approx 4.7 \ln \beta' - 6.5. \quad (66)$$

Empirically, we still observe this behavior on average for SP2 when $\mu' \neq \phi$ provided μ' is close to 0.5.

However, while this condition gives a minimum bound for layers needed to meet the slope requirement, it does not mean accuracy plateaus once this layer count is met. As Fig. 6 shows, beyond some baseline level, accuracy can further increase with expressibility or number of parameters, either by architecture change such as MaxSP2 or additional layers for MLSP2-but this is unnecessary in the regime where numerical precision is the dominant cause of error, as opposed to error in the underlying model (see Fig. 8).

C. Region of Validity By Layer Count

If $0 < \mu' < 1/2$, the inequalities of Eq. (48) can be used to bound β' by

$$2\mu_0\beta_0 \geq \beta' \quad \text{and} \quad (1 - \mu_0)\beta_0 \geq \beta'. \quad (67)$$

Since both inequalities need to be satisfied, the bounds are maximal when $\mu_0 = 1/3$, leading to

$$\beta' \leq \frac{2}{3}\beta_0. \quad (68)$$

Making use of the symmetry of f

$$f(x'; \beta', \mu') = 1 - f(1 - x'; \beta', 1 - \mu'), \quad (69)$$

on the unit interval gives the same bound for all $0 < \mu' < 1$. By also using Eq. (65), we are able to deduce that for any desired layer count n_ℓ , a model can be trained at:

$$\beta_0 = 4(2\phi)^{n_\ell}, \quad \mu_0 = \frac{1}{3}, \quad (70)$$

that can then be used with any $0 < \mu' < 1$ and $0 < \beta' \leq \frac{2}{3}\beta_0$ while still maintaining the same accuracy as the model at (β_0, μ_0) . This makes it possible to train a single set of coefficients (or, weights) that is usable for a wide range of temperatures and chemical potentials. For example, one could train a 10 layer model up to $\beta_0 = 33.3$, and thus use only 10 layers for any Fermi evaluation up to $\beta' = 22.2$.

Going back to the $\beta_0 = 1500$ and $\mu_0 = 1/3$ model from Sec. IV 1, we now see that these parameter choices enable model use for all $0 < \beta' \leq 1000$ and all valid μ' , i.e. $0 < \mu' < 1$. By Eq. (48) and the fact that $\beta = 1/k_B T$, this model can therefore handle a temperature as low as

$$T \geq \frac{(\varepsilon_{\max} - \varepsilon_{\min})}{k_B \times 1000} = 11.6(\varepsilon_{\max} - \varepsilon_{\min}) \text{ K}. \quad (71)$$

So if the spectral width of H is on the order of 1 eV, the model can very accurately capture temperatures as low as 11.6 K. However if the spread in energies is on the order of 100 eV, the model cannot reliably go below 1160 K and capturing lower temperatures would require a new model be trained at a higher β_0 .

D. Comparison to Diagonalization

For numerical comparisons, we focus on the MLSP2 method. Using random, symmetric Hamiltonian matrices we compute the single-particle density matrix using both diagonalization and MLSP2, and then compare wall clock times. Our experiments were run on an Nvidia RTX 6000 Ada GPU and use both single and double precision for diagonalization, and our mixed precision Tensor Core approach from Sec. V A for MLSP2. The MLSP2 model was trained at parameters $\beta_0 = 1500$ and $\mu_0 = 1/3$ and the number of layers was calculated using Eq. (66)

and resulted in 24 layers. With this number of layers, the overall model error was less than the single precision unit-roundoff of 2^{-24} .

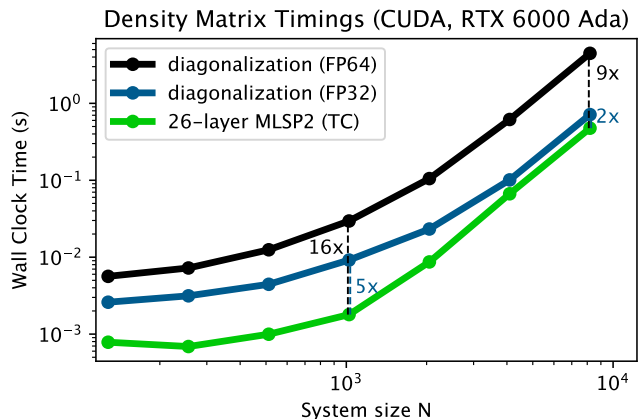


FIG. 7. Wall clock time for a 26-layer MLSP2 evaluation (up to $\beta' \leq 1000$) using Nvidia Tensor Cores compared to the single and double precision cuSolver divide-and-conquer diagonalization, `cusolverDn<T>syevd`, on an Nvidia RTX 6000 Ada.

The results seen in Fig. 7 confirm that MLSP2 evaluated using Nvidia Tensor Cores offer significant speed ups over diagonalization-based density matrix construction. Diagonalization was evaluated using `cusolverDn<T>syevd`, which does not use Tensor Cores. `<T>` can be either `D` or `S` for double or single precision, respectively. At intermediate matrix sizes, the figure shows a 16x speed for MLSP2 over a double precision diagonalization-based density matrix construction, and a 9x speed up for larger matrix sizes.

Comparing to single precision diagonalization instead results in smaller speed ups of 5x and 2x. However, the diagonalization algorithm can be unreliable in single precision, sometimes producing much larger errors than MLSP2 when compared to double precision diagonalization, or diverging entirely, with no flag or indication of failure. Thus it is reasonable to consider double precision diagonalization as the more meaningful comparison.

The performance gains described are hardware dependent. An Nvidia RTX 6000 Ada has a peak Tensor Core performance of about 180 Tflops for FP16 data,⁴⁷ whereas regular, single-precision (non-Tensor-Core) performance on this device is about 90 Tflops. This results in a Tensor Core to single-precision performance ratio of about 2:1. On more high-performance computing oriented devices, such as an Nvidia H100, this ratio is closer to 15:1.⁴⁸ We thus expect a much greater performance difference in favor of MLSP2 on these kinds of devices.

Our speed advantage comes at an accuracy tradeoff. When competing with high-performance diagonalization routines, accuracy is determined not only from the model accuracy, as seen in Fig. 8, but also from the underlying

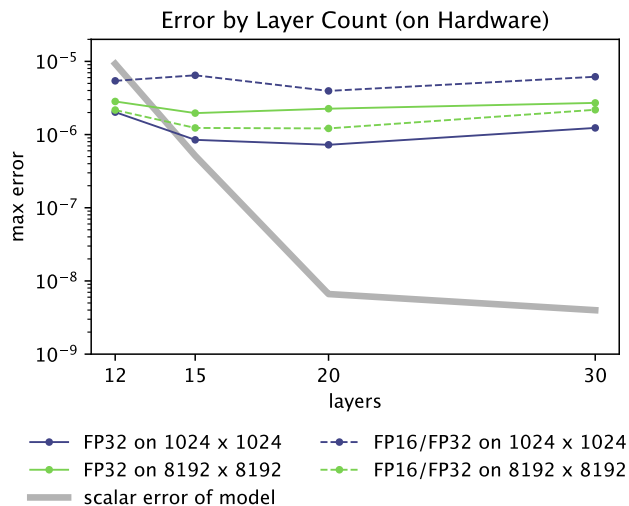


FIG. 8. Model error compared to our accelerated mixed precision algorithm on Tensor Cores (dashed lines) and standard single precision (solid lines). We hit the maximum possible accuracy at relatively few layers. The model was trained at $\beta_0 = 40$, $\mu_0 = 0.3$.

precision used in the matrix multiplication implementation. In the case of using single precision or the Tensor Core implementation from Sec. V A in our models, we are limited to accuracies between 10^{-5} and 10^{-6} (measured in the 2-norm), regardless of how accurate the underlying model is.

Practically, some of the advantage is also dampened by the need to iteratively determine μ in the case when it is not known a priori, as it is defined implicitly through the sum of the fractional occupation numbers equaling the occupation number. Computing the density matrix with diagonalization, however, only requires a single diagonalization. This is because the energies, ε_i , are then known and we only need to solve the one-dimensional equation $\sum_i f_i = \text{Tr}(D) = N_{occ}$ to compute the unknown μ . Nevertheless, as long as the number of iterations for determining μ is small, typically 1 or 2 in many practical simulations, we expect to maintain a sizable speed advantage over diagonalization.

VI. CONCLUSION

We have developed several finite-temperature recursive Fermi-operator expansion based on the zero-temperature second-order spectral projection (SP2) method, thereby generalizing SP2 to finite electronic temperatures. The expansion coefficients are determined using machine learning models that offer different levels of expression and computational cost. Furthermore, once a model is trained for a sufficiently high inverse temperature, the model becomes robustly transferrable and can be used in an entire region of normalized parameter space called

the region of validity. This makes our models a convenient choice for dynamical finite temperature simulations, such as quantum molecular dynamics, where the chemical potential or electronic temperature may fluctuate between timesteps. Our approach avoids the need for diagonalization and relies solely on highly optimized matrix-matrix multiplication kernels. We demonstrate how these schemes can be implemented and applied to construct density matrices on modern GPUs and dense matrix multiply units (e.g. Tensor Cores) showcasing large speedups relative to vendor optimized diagonalization routines. High performance CUDA implementations of MLSP2, including the affine rescaling and determination of μ via Newton’s method, are contained in the `/src/gpu/` directory within the github repository: <https://github.com/lanl/sedacs>.

ACKNOWLEDGMENTS

This work is supported by the U.S. Department of Energy, Office of Basic Energy Sciences (FWP LANLE8AN) and by the Laboratory-Directed Research and Development Program (20240006DR) at Los Alamos National Laboratory (LANL). LANL is operated by Triad National Security, LLC, for the National Nuclear Security Administration of the U.S. Department of Energy Contract No. 892333218NCA000001. This document has LA-UR number LA-UR-26-22648.

AUTHOR DECLARATIONS

The authors have no conflict of interest to disclose.

DATA AVAILABILITY

All codes, including neural network weights and the mechanism for their generation, are included in the text, appendix, or supporting information.

REFERENCES

- ¹P. Hohenberg and W. Kohn, Phys. Rev. **136**, B:864 (1964).
- ²W. Kohn and L. J. Sham, Phys. Rev. **140**, 1133 (1965).
- ³R. G. Parr and W. Yang, *Density-functional theory of atoms and molecules* (Oxford University Press, Oxford, 1989).
- ⁴R. Dreizler and K. Gross, *Density-functional theory* (Springer Verlag, Berlin Heidelberg, 1990).
- ⁵D. Marx and J. Hutter, “Modern methods and algorithms of quantum chemistry,” (2000).
- ⁶G. Golub and C. F. van Loan, *Matrix Computations* (Johns Hopkins University Press, Baltimore, 1996).
- ⁷S. Goedecker, Rev. Mod. Phys. **71**, 1085 (1999).
- ⁸A. M. N. Niklasson, “Density matrix methods in linear scaling electronic structure theory,” in *Linear-Scaling Techniques in Computational Chemistry and Physics: Methods and Applications*, edited by R. Zalesny, M. G. Papadopoulos, P. G. Mezey,

- and J. Leszczynski (Springer Netherlands, Dordrecht, 2011) pp. 439–473.
- ⁹D. R. Bowler and T. Miyazaki, *Rep. Prog. Phys.* **75**, 036503 (2012).
- ¹⁰W. Yang, *Phys. Rev. Lett.* **66**, 1438 (1991).
- ¹¹W. T. Yang and T. S. Lee, *J. Chem. Phys.* **103**, 5674 (1995).
- ¹²K. Kitaura, E. Ikeo, T. Nakano, and M. Uebayasi, *Chem. Phys. Lett.* **313**, 701 (1999).
- ¹³Y. Nishimoto, D. G. Fedorov, and S. Irle, *J. Chem. Theory Comput.* **10**, 4801 (2014).
- ¹⁴A. H. R. Palser and D. E. Manolopoulos, *Phys. Rev. B* **58**, 12704 (1998).
- ¹⁵K. Nemeth and G. E. Scuseria, *J. Chem. Phys.* **113**, 6035 (2000).
- ¹⁶A. Holas, *Chem. Phys. Lett.* **340**, 552 (2001).
- ¹⁷A. M. N. Niklasson, *Phys. Rev. B* **66**, 155115 (2002).
- ¹⁸A. M. N. Niklasson, *Phys. Rev. B* **68**, 233104 (2003).
- ¹⁹D. K. Jordan and D. A. Mazziotti, *J. Chem. Phys.* **122**, 084114 (2005).
- ²⁰E. Rudberg and E. H. Rubensson, *J. Phys.: Condens. Matter* **23**, 075502 (2011).
- ²¹P. Suryanarayana, *Chem. Phys. Lett.* **555**, 291 (2013).
- ²²E. H. Rubensson and A. M. N. Niklasson, *SIAM J. Sci. Comput.* **36**, 148 (2014).
- ²³L. A. Truflandier, R. M. Dianzinga, and D. R. Bowler, *JOURNAL OF CHEMICAL PHYSICS* **144** (2016), 10.1063/1.4943213.
- ²⁴S. M. Mniszewski, R. Perriot, E. H. Rubensson, C. F. A. Negre, M. J. Cawkwell, and A. M. N. Niklasson, *Journal of Chemical Theory and Computation* **15**, 190 (2019), pMID: 30452247, <https://doi.org/10.1021/acs.jctc.8b00887>.
- ²⁵S. Goedecker, *Rev. Mod. Phys.* **71**, 1085 (1999).
- ²⁶A. Weiße, G. Wellein, A. Alvermann, and H. Fehske, *Reviews of modern physics* **78**, 275 (2006).
- ²⁷J. Finkelstein, C. F. Negre, and J.-L. Fattebert, *The Journal of Chemical Physics* **159** (2023).
- ²⁸M. S. Paterson and L. J. Stockmyer, *SIAM Rev.* **45**, 3 (1973).
- ²⁹W. Z. Liang, C. Saravanan, Y. Shao, R. Baer, A. T. Bell, and M. Head-Gordon, *J. Chem. Phys.* **119**, 4117 (2003).
- ³⁰M. J. Cawkwell, E. J. Sanville, S. M. Mniszewski, and A. M. N. Niklasson, *Journal of Chemical Theory and Computation* **8**, 4094 (2012), pMID: 26605576, <https://doi.org/10.1021/ct300442w>.
- ³¹P. Steinbach and C. Bannwarth, *Journal of Chemical Theory and Computation* **21**, 7335 (2025), pMID: 40662608, <https://doi.org/10.1021/acs.jctc.5c00262>.
- ³²J. Finkelstein, J. S. Smith, S. M. Mniszewski, K. Barros, C. F. A. Negre, E. H. Rubensson, and A. M. N. Niklasson, *Journal of Chemical Theory and Computation* **17**, 2256 (2021), pMID: 33797253, <https://doi.org/10.1021/acs.jctc.1c00057>.
- ³³J. Finkelstein, J. S. Smith, S. M. Mniszewski, K. Barros, C. F. A. Negre, E. H. Rubensson, and A. M. N. Niklasson, *Journal of Chemical Theory and Computation* **17**, 6180 (2021), pMID: 34595916, <https://doi.org/10.1021/acs.jctc.1c00726>.
- ³⁴N. D. Mermin, *Phys. Rev. B* **137**, A1441 (1965).
- ³⁵A. Kruchinina, E. Rudberg, and E. H. Rubensson, *Journal of Chemical Theory and Computation* **12**, 5788 (2016), pMID: 27783507, <https://doi.org/10.1021/acs.jctc.6b00626>.
- ³⁶H. Li, Z. Xu, G. Taylor, C. Studer, and T. Goldstein, *Advances in Neural Information Processing Systems*, *Advances in Neural Information Processing Systems (NeurIPS)* **31** (2018).
- ³⁷G. Huang, Z. Liu, L. Van Der Maaten, and K. Q. Weinberger, in *2017 IEEE Conference on Computer Vision and Pattern Recognition (CVPR)* (2017) pp. 2261–2269.
- ³⁸A. M. N. Niklasson, M. J. Cawkwell, E. H. Rubensson, and E. Rudberg, *Phys. Rev. E* **92**, 063301 (2015).
- ³⁹M. K. Transtrum and J. P. Sethna, “Improvements to the levenberg-marquardt algorithm for nonlinear least-squares minimization,” (2012), arXiv:1201.5885 [physics.data-an].
- ⁴⁰J. Myles White and P. K. Mogensén, “LsqFit.jl,” (2019).
- ⁴¹A. Pal, F. Holtorf, A. Larsson, T. Loman, Utkarsh, F. Schäfer, Q. Qu, A. Edelman, and C. Rackauckas, *ACM Trans. Math. Softw.* (2025), 10.1145/3779117, just Accepted.
- ⁴²K. Jordan, Keller Jordan Blog (2024).
- ⁴³A. M. N. Niklasson, *J. Chem. Phys.* **129**, 244107 (2008).
- ⁴⁴cuBLAS authors, *cuBLAS 13.1 Docs*, Tech. Rep. (2026).
- ⁴⁵H. Ootomo, K. Ozaki, and R. Yokota, *The International Journal of High Performance Computing Applications* **38**, 297 (2024).
- ⁴⁶M. Fasi, N. J. Higham, M. Mikaitis, and S. Pranesh, *PeerJ Computer Science* **7**, e330 (2021).
- ⁴⁷*Nvidia Ada Lovelace Professional GPU Architecture*, Nvidia Corporation (2022), note: from Appendix A, comparing “Peak FP16 Tensor TFLOPS with FP32 Accumulation” to “Peak FP32 TFLOPS (non-Tensor)”.
- ⁴⁸*Nvidia H100 Tensor Core GPU Data Sheet*, Nvidia Corporation (2024), note: comparing FP16 Tensor Core TFLOPS (without sparsity) to FP32 TFLOPS.
- ⁴⁹S. Batzner, A. Musaelian, L. Sun, M. Geiger, J. P. Mailoa, M. Kornbluth, N. Molinari, T. E. Smidt, and B. Kozinsky, *Nature Communications* **13**, 2453 (2022).
- ⁵⁰A. E. A. Allen, E. Shinkle, R. Bujack, and N. Lubbers, *npj Computational Materials* (2026), 10.1038/s41524-025-01948-0.
- ⁵¹Y. Xu and H. Zhang, *IEEE Trans. Inf. Theor.* **70**, 7125–7142 (2024).
- ⁵²K. He, X. Zhang, S. Ren, and J. Sun, arXiv preprint arXiv:1512.03385 (2015).

Appendix A: MLSP2 python implementation

Here we present a working Python implementation of MLSP2 complete with trained model coefficients for $\beta_0 = 1500$ and $\mu_0 = 1/3$. This code uses double precision and needs to be properly adapted to take advantage of the mixed-precision formulation presented in the main text.

```

1 import numpy as np
2
3 # Model Weights for MLSP2 defined at beta_0 = 1500, mu_0 = 1/3
4
5 #         theta_{i,1}           theta_{i,2}           theta_{i,3}           theta_{i,4}
6 weights = [
7 [ -1.353996666080607e+00, +2.437540893737664e+00, -2.038466804171965e-01, +1.291156147536192e-11 ],
8 [ +1.608677030263155e+00, -2.987544634415441e-01, -6.746741346599809e-02, -7.006084032292678e-12 ],
9 [ -2.351636735892118e+00, +2.613813908880740e+00, -2.081115324436639e-03, -6.572840812953572e-13 ],
10 [ +1.810031371507046e+00, -3.733036049410451e-02, -5.442179841399564e-02, +4.318503541775794e-11 ],
11 [ -2.732204264661287e+00, +2.825886342002125e+00, +8.167975559885774e-03, -1.662456055798004e-11 ],
12 [ -1.873987421378235e+00, +2.138798318408699e+00, +3.573114610928145e-02, +4.542623791264443e-12 ],
13 [ +1.402261079424850e+00, +4.890736627204146e-02, -4.237220339751432e-02, +2.424648524635838e-11 ],
14 [ +1.713089400763156e+00, -1.034037621506357e-01, -2.438094942357169e-02, +7.873381643056254e-11 ],
15 [ -3.252595736449542e+00, +2.628649626717414e+00, +3.165347918592593e-02, -6.312379678783267e-11 ],
16 [ -1.878046620274372e+00, +2.074880349608742e+00, +3.449163838903798e-02, -6.649574392039178e-11 ],
17 [ +1.310464008049612e+00, +5.496499701340592e-02, +3.310087064751345e-03, +2.825980776677432e-10 ],
18 [ +1.563608995897714e+00, -8.606990671650539e-03, -1.301065468049911e-02, -1.424083924407828e-07 ],
19 [ -3.038983738437103e+00, +2.477686862799397e+00, +2.636871201950337e-02, -1.330100571490071e-07 ],
20 [ -1.699377329573085e+00, +2.076565284757246e+00, +3.442469802192470e-02, +4.896446563691430e-03 ],
21 [ +1.256940670391469e+00, +5.777573303514125e-02, +4.902596975631270e-02, -2.302054912581413e-03 ],
22 [ -1.390281989291434e+00, +1.966243706278270e+00, +1.910503489826946e-02, +1.606259300834474e-02 ],
23 [ +1.172415492052006e+00, +2.982302801604828e-02, +4.530045685625948e-02, -1.539021333689731e-02 ],
24 [ +1.351448045975672e+00, +5.773064380022182e-02, +3.753306163777001e-02, -1.276795931125504e-01 ],
25 [ -1.212734900653146e+00, +1.861660915086903e+00, +1.242573869144004e-02, -1.100276149057915e-01 ],
26 [ +8.610663421144649e-01, +1.048747203546148e-02, +4.701135000272372e-02, -4.946843804326570e-02 ],
27 [ -1.369173339062334e+00, +1.699077704335121e+00, -7.732969926664974e-03, -1.761228530611925e-01 ],
28 [ -1.452079661340262e+00, +1.993171071701545e+00, -1.661115887219701e-02, -5.688902388963853e-01 ],
29 [ +1.347262922911275e+00, +2.198074427424086e-02, +1.995615256168758e-01, +5.964487309001580e-01 ],
30 [ -1.114238353358810e+00, +1.896937623313116e+00, -7.280733281872145e-02, +1.530915295291056e+00 ],
31 [ +9.411010738180853e-01, -1.554719335561439e-01, +6.584253835393120e-02, -2.059339861429303e-01 ],
32 [ +8.321693583250559e-01, +5.698259888759222e-01, -4.234806053199446e-01, +5.698259888760550e-01 ]
33 ]
34
35 beta0, mu0 = 1500, 1/3
36
37 # Gershgorin circle theorem providing minimum and maximum bounds for a real spectrum
38 def Gershgorin(A):
39
40     # extract diagonal entries of matrix (NOT diagonalization)
41     D = np.diag(A)
42
43     # radii of Gershgorin circles for each row
44     R = np.sum(np.abs(A),axis=1) - np.abs(D)
45
46     # return minimum and maximum of all bounds of all circles
47     return np.min(D-R), np.max(D+R)
48
49 # defined for (emax - emin) * beta < 1000, emin < mu < emax
50 def mlsp2(H, beta, mu):
51
52     # estimate bounds on spectrum of true H
53     emin, emax = Gershgorin(H)
54
55     # Identity matrix
56     I = np.eye(H.shape[0])
57
58     # primed variables given by Eqs. 41 - 43
59     H_prime = (emax * I - H)/(emax - emin)
60     mu_prime = (emax - mu)/(emax - emin)
61     beta_prime = (emax - emin) * beta
62
63     # condition for validity by Eq. 65
64     assert beta_prime <= (2/3) * beta0

```

```

65     assert emin < mu < emax
66
67     # flip given by Eq. 67 if mu' > 0.5
68     mu_switch = mu_prime > 0.5
69     if mu_switch:
70         H_prime = I - H_prime
71         mu_prime = 1 - mu_prime
72
73     # H0 given by Eq. 46
74     X = (H_prime - mu_prime * I)*(beta_prime/beta0) + mu0 * I
75     A = np.zeros_like(X)
76
77     # MLSP2 as given by Eq. 22
78     for a,b,c,d in weights:
79         A += d * X
80         X = a * np.matmul(X,X) + b * X + c * I
81         # for faster routines in cuBLAS see Sec. V Numerics
82
83     # corresponding flip given by Eq. 46
84     return I - (A + X) if mu_switch else (A + X)
85
86
87 # test cases
88 if __name__ == '__main__':
89
90     for i in range(10):
91
92         # seed random number generation for reproducibility and fix matrix size
93         rng = np.random.default_rng(seed=i)
94         N = 100
95
96         # generate random matrix of size (N,N) and make it symmetric
97         H = rng.uniform(0, 1, (N,N))
98         H = H + H.T
99
100        # estimate spectral bounds
101        emin, emax = Gershgorin(H)
102
103        # choose beta and mu such that beta' and mu' fall inside region of validity
104        beta = rng.uniform(1, (2/3 * beta0)/(emax - emin))
105        mu = rng.uniform(emin, emax)
106
107        # construct density matrix with MLSP2
108        D_mlsp2 = mlsp2(H, beta, mu)
109
110        # compare to diagonalization
111        evals, evecs = np.linalg.eigh(H)
112        occupation = 1 / (1 + np.exp(beta * (evals - mu)))
113        D_diag = (evecs * occupation) @ evecs.T
114
115        # print matrix 2-norm of error (maximal eigenvalue difference)
116        print( np.linalg.norm(D_diag - D_mlsp2, ord=2) )

```

Appendix B: Analysis of Spectral Refinement Networks

Application of matrix polynomials preserves the (identical) left and right eigenspaces of a Hermitian H , so implementing the spectral projection scheme with learned weights can be thought of as defining a deep neural network with some extent of equivariance. This is not equivariance in the sense of Equivariant Neural Networks⁴⁹ defined as commuting with a fixed symmetry group G . By that definition, the network $f : X \rightarrow Y$ going from a vector space X to a vector space Y is G -equivariant if

it satisfies

$$f(D_X[g]x) = D_Y[g]f(x), \quad \forall x \in X, \forall g \in G. \quad (\text{B1})$$

That is, for every element g of group G , the function application commutes with the representations $D_V[g]$ of g in each vector space $V \in \{X, Y\}$. However, our network commutes with similarity transformations S on H ,

$$f(SHS^{-1}) = Sf(H)S^{-1}. \quad (\text{B2})$$

These can be considered as a form of equivariance in the sense of equation B1 over the real vector space of

Hermitian matrices,

$$\vec{f}((S \otimes S^{-1})\text{vec}(H)) = (S \otimes S^{-1})\vec{f}(\text{vec}(H)), \quad (\text{B3})$$

where the representations respected are fundamental, simply elements of the group of similarity transformations on H . However, this group is dependent on the input H , and is thus not some fixed group G . The network also clearly is not *invariant*,⁵⁰ as applying similarity transformations changes the output. Our method even further deviates from traditional neural networks, whose convergence proofs⁵¹ are generally based on Lipschitz continuity, which our network does not formally have, as our nonlinearity is squaring, which has unbounded derivative on the real line. However, the inputs to each layer can empirically be seen to be within $\epsilon \approx 0.5$ of the initial and final range $[0, 1]$, which is expected as each layer is only a slight alteration of the initial spectral refinement technique, which is formally bound within that range. This ensures Lipschitz continuity and thus at minimum convergence in the same manner as such networks, but we observe far stronger convergence behavior in layer count, and much faster convergence in training by using methods designed for curve-fitting tasks: rootfinding. Because we have a weight initialization (the embedding of traditional SP2) already very close to a solution, rootfinding methods such as nonlinear least squares³⁹ display rapid convergence with such steps.

Although we see some key distinctions between traditional deep learning approaches and our ‘‘Spectral Refinement Networks,’’ many principles of deep learning still apply to our models, especially concerning expressivity. We show that using fully connected layers in this architecture appreciably improves model accuracy vs layer count, seen in Fig. 6, very similarly to how it does in CNNs.³⁷ More generally, parsimoniously introducing skip connections as in ResNet⁵² can substantially improve the expressibility of the model without adding as severe memory requirements as full connectivity, while maintaining such theoretical benefits as smoothing the loss landscape.³⁶ Thus, drawing inspiration from machine learning, one can construct several families of such spectral networks, with increasing numbers of parameters (but also increasing memory requirements) that increase the accuracy of approximation at a given layer count.

Appendix C: Model Embeddings (SP2 \subset MLSP2 \subset Skip-SP2 \subset MaxSP2 \subset ArbSP2)

Each of the following correspondences is quite useful not only analytically in showing hierarchies of expressibility, but also numerically, as it provides stable initial guesses, test cases, and benchmarks of errors introduced by changing the algorithm without changing the corresponding weights. Initial guesses are, in particular, extremely important, as they are minimally changed by the optimization process but lead to extreme gains in accuracy depending on the number of parameters available

for fine tuning. We do not know whether different initial guesses from a less expressive model cause a more expressive model to fall into different basins of attraction in parameter space, and these relations can prove extremely useful in investigating that.

Obviously, we can show SP2 \subset MLSP2 with the relation

$$\theta_{i+1,1\dots 3} = \begin{cases} \{1, 0, 0\} & \text{if } |\mu_i^2 - \mu'| < |2\mu_i^2 - \mu_i^2 - \mu'| \\ \{-1, 2, 0\} & \text{otherwise,} \end{cases}$$

$$\theta_{i,4} = \begin{cases} 1 & \text{if } i = n \\ 0 & \text{otherwise.} \end{cases} \quad (\text{C1})$$

Showing MLSP2 \subset Skip-SP2 is perhaps the most nuanced, as it involves going from an arbitrary quadratic to squaring an affine combination, which means certain terms must be shifted to the accumulator, and the linear combination must have an added constant term (hence, affine). Let’s redefine, for convenience, MLSP2 as

$$x_{i+1} = a_i x_i^2 + b_i x_i + c_i,$$

$$A = \sum_{i=0}^n d_i x_i. \quad (\text{C2})$$

We wish to put it into the form

$$\tilde{x}_{i+1} = (\alpha_{i,k} + \alpha_{i,0} \tilde{x}_i + \beta_{i,1} A_{i,1})^2,$$

$$A = A_0 + \sum_{i=0}^n \gamma_i \tilde{x}_i, \quad (\text{C3})$$

using $k = 1$ and $K = 1$. It’s clear that $\beta_{i,j} = 0$, and indeed, if we have

$$x_0 = \tilde{x}_0 = 1 - x, \quad (\text{C4})$$

we can define

$$\tilde{x}_{i+1} = \left(x_i + \frac{b_i}{2a_i}\right)^2 = x_i^2 + \frac{b_i}{a_i} x_i + \frac{b_i^2}{4a_i^2}. \quad (\text{C5})$$

Then, x_{i+1} can be put in terms of \tilde{x}_{i+1} :

$$x_{i+1} = a_i \tilde{x}_{i+1} - \frac{b_i^2}{4a_i} + c_i. \quad (\text{C6})$$

This definition is, of course, doubly recursive, but we can compactify it:

$$\tilde{x}_{i+1} = \left(a_{i-1} \tilde{x}_i - \frac{b_{i-1}^2}{4a_{i-1}} + c_{i-1} + \frac{b_i}{2a_i}\right)^2. \quad (\text{C7})$$

Thus, we have

$$\alpha_{i,k} = -\frac{b_{i-1}^2}{4a_{i-1}} + c_{i-1} + \frac{b_i}{2a_i} \quad (\text{C8})$$

$$\alpha_{i,0} = a_{i-1}.$$

Similarly, we have

$$\begin{aligned} A &= A_0 + \sum_{i=0}^N d_i x_i \\ &= A_0 + \sum_i d_i \left(a_{i-1} \tilde{x}_i - \frac{b_{i-1}^2}{4a_{i-1}} + c_{i-1} \right). \end{aligned} \quad (\text{C9})$$

This gives

$$\begin{aligned} \gamma_i &= d_i a_{i-1} \\ A_0 &= \sum_j d_j \left(c_{j-1} - \frac{b_{j-1}^2}{4a_{j-1}} \right) \end{aligned} \quad (\text{C10})$$

The alternative form of MLSP2, Eq. (24), is easiest to show from the above embedding in Skip-SP2. We require simply to factor out $\alpha_{i,0}$ from every intermediate expression. Indeed, we have the embedding in Skip-SP2

$$\tilde{x}_{i+1} = (\alpha_{i,k} + \alpha_{i,0} \tilde{x}_i)^2 = \alpha_{i,0}^2 \left(\frac{\alpha_{i,k}}{\alpha_{i,0}} + \tilde{x}_i \right)^2. \quad (\text{C11})$$

If we allow every layer x_i of MLSP2 to vary from \tilde{x}_i by some multiplicative factor, i.e. $s_i x_i = \tilde{x}_i$, then we can write

$$\begin{aligned} s_{i+1} x_{i+1} &= \alpha_{i,0}^2 \left(\frac{\alpha_{i,k}}{\alpha_{i,0}} + s_i x_i \right)^2 \\ &= \alpha_{i,0}^2 s_i^2 \left(\frac{\alpha_{i,k}}{\alpha_{i,0} s_i} + x_i \right)^2. \end{aligned} \quad (\text{C12})$$

By setting $s_{i+1} = \alpha_{i,0}^2 s_i^2$, we see that $\theta_{i,1} = \alpha_{i,k}/(\alpha_{i,0} s_i)$ and $\theta_{i,2} = \gamma_i s_i$ satisfy both the above and Eq. (24):

$$\begin{aligned} x_{i+1} &= \left(\frac{\alpha_{i,k}}{\alpha_{i,0} s_i} + x_i \right)^2 \\ A_{i+1} &= A_i + \gamma_i s_i x_i. \end{aligned} \quad (\text{C13})$$

The final loose ends are $\theta_{n,1} = A_0$ and $\theta_{n,2} = \gamma_n s_n$. Skip-SP2 \subset MaxSP2 is given by

$$\begin{aligned} \delta_i &= \left(\sum_{j=1}^K \beta_{i,j} A_{0,j} \right) + \alpha_{i,k} \\ \theta_{i,j} &= \left(\sum_{l=1}^K \beta_{i,l} \gamma_{j,l} \right) + \begin{cases} \alpha_{i,n-j} & \text{if } j \geq n-k \\ 0 & \text{otherwise.} \end{cases} \end{aligned} \quad (\text{C14})$$

Finally, MaxSP2 \subset ArbSP2 is trivial, and has an additional degree of freedom for every layer: $c_i \psi_{i,j} = c_i^{-1} \phi_{i,j} = \theta_{i,j}$, where c_i are arbitrary scalars that can be introduced to break symmetry.

1. Eigenvalues of $\phi_n \psi_n^\top$

Each layer of ArbSP2 as described by equation 28 can be considered a quadratic form $\phi_n \psi_n^\top$ in the vector of all

previous layer outputs, x_n . To be specific, when operating on scalars, $x_n \in \mathbb{R}^n$, and when operating on matrices x_n is a module over the (abelian) ring of matrix polynomials in H , but the analysis proceeds identically as in the case of real numbers, so we shall consider it as such. The expressivity of this architecture is tied intrinsically to the rank of this quadratic form, which we examine below.

The rank-one matrix $\mathbf{u}\mathbf{v}^\top$ has one (right) eigenvector $\hat{\mathbf{u}}$, with $\lambda = \mathbf{u} \cdot \mathbf{v}$, but when it is considered as a quadratic form, only its symmetric part, $\frac{1}{2}(\mathbf{u}\mathbf{v}^\top + \mathbf{v}\mathbf{u}^\top)$ acts on the input (the input is applied from both the left and the right, and thus the antisymmetric component $\mathbf{x}^\top \frac{1}{2}(\mathbf{u}\mathbf{v}^\top - \mathbf{v}\mathbf{u}^\top)\mathbf{x}$ cancels). This component, however, has two eigenvalues, which can be found by applying a similarity transformation that puts the matrix in block-diagonal form, in the basis of $\{\mathbf{u}, \mathbf{v}\}$ and additional directions that map to 0. In this basis, the nonzero block is

$$M = \frac{1}{2} \begin{bmatrix} \langle \mathbf{u}, \mathbf{v} \rangle & \langle \mathbf{v}, \mathbf{v} \rangle \\ \langle \mathbf{u}, \mathbf{u} \rangle & \langle \mathbf{u}, \mathbf{v} \rangle \end{bmatrix}, \quad (\text{C15})$$

whose eigenvalues can be found by $\text{tr}M = \langle \mathbf{u}, \mathbf{v} \rangle$ and $\det M = \frac{1}{4} (\langle \mathbf{u}, \mathbf{v} \rangle^2 - \langle \mathbf{u}, \mathbf{u} \rangle \langle \mathbf{v}, \mathbf{v} \rangle)$. This gives

$$\begin{aligned} \lambda &= \frac{\text{tr}M \pm \sqrt{(\text{tr}M)^2 - 4 \det M}}{2} \\ &= \frac{1}{2} \left(\langle \mathbf{u}, \mathbf{v} \rangle \pm \sqrt{\langle \mathbf{u}, \mathbf{u} \rangle \langle \mathbf{v}, \mathbf{v} \rangle} \right), \end{aligned} \quad (\text{C16})$$

which are necessarily the same as the eigenvalues of the original matrix, because similarity transformations preserve eigenvalues.

Thus, despite requiring only one general matrix-matrix multiplication, $\phi_n \psi_n^\top$ as a quadratic form is rank 2, and thus cannot be reduced to a single squaring (rank 1). This nearly doubles expressivity versus layer count, but requires arbitrary multiplication and not squaring – a more expensive nonlinearity on specialized hardware. On Nvidia devices making full use of mixed precision arithmetic, matrix multiplications of this type are 50% more expensive than squaring symmetric matrices on a flop basis, which can be seen by adapting the algorithm in Section V A for the multiplication of two matrices A, B . This therefore sacrifices polynomial order achievable with a fixed number of hardware multiplications, which nonetheless may be useful at low β (high temperature systems), where the cutoff is not so steep, and thus the dominant factor in the approximation accuracy is not simply polynomial order.

2. Symmetry Breaking

Propagating gradients through a layer of equation 28 results in

$$\begin{aligned}\bar{\phi}_{i,j} &= \bar{x}_{i+1} \frac{\partial x_{i+1}}{\partial \phi_{i,j}} \\ &= \bar{x}_{i+1} \left(\sum_{l \leq i} \psi_{i,l} x_l \right) x_j.\end{aligned}\quad (\text{C17})$$

Likewise for ψ_i ,

$$\bar{\psi}_{i,j} = \bar{x}_{i+1} \left(\sum_{l \leq i} \phi_{i,l} x_l \right) x_j.\quad (\text{C18})$$

If the weights for Arbitrary Multiplication are naively initialized as the embedding of MaxSP2, i.e. $\phi_i = \psi_i = \theta_i$, then we see a critical issue. Equations C17 and C18 become equal, so any optimization performed on ϕ, ψ will continue to keep them equal. However, the embedding of MaxSP2 into Arbitrary Multiplication has a particular ‘‘gauge freedom:’’ $c_i \phi_i = c_i^{-1} \psi_i = \theta_i$ results in an identical model (the constant factors can be factored out of the sums and cancel upon multiplication of the resultants). This cancellation ensures the first iteration will have identical $\frac{\partial x_{m>n}}{\partial x_{n+1}}$, and thus identical \bar{x}_{n+1} , but fundamentally differ in the second term. Comparing to the gradients in MaxSP2, we can reduce C17-C18 to

$$\begin{aligned}\bar{\theta}_{i,j} &= 2\bar{x}_{i+1} \left(\sum_{l \leq i} \theta_{i,l} x_l \right) x_j \\ \bar{\phi}_{i,j} &= \frac{1}{2} c_i \bar{\theta}_{i,j} \\ \bar{\psi}_{i,j} &= \frac{1}{2} c_i^{-1} \bar{\theta}_{i,j},\end{aligned}\quad (\text{C19})$$

which breaks our symmetry by causing ϕ and ψ to evolve at rates inversely proportional to their initial proportionality to θ . Note that if $c_i \neq 1$, equation C19 is only valid for the first step, after which symmetry breaks and ϕ_i, ψ_i are no longer proportional to θ_i .

Appendix D: Quadratic Convergence of SP2 when using repeated applications of $f_1 \circ f_0$

If $0 < x < \varphi^{-1}$, and $F = f_1 \circ f_0$,

$$\begin{aligned}|F(x) - \Theta(\varphi^{-1} - x)| \\ &= |F(0) + F'(0)x + F''(0)x^2 - 0| \\ &= 2x^2,\end{aligned}\quad (\text{D1})$$

so that if $x_n = F \circ \dots \circ F(x)$ is n -th application of F at x ,

$$\begin{aligned}|x_{n+1} - \Theta(\varphi^{-1} - x)| &= |F(x_n) - \Theta(\varphi^{-1} - x)| \\ &= 2(x_n - \Theta(\varphi^{-1} - x))^2,\end{aligned}\quad (\text{D2})$$

and $x_n \rightarrow 0$ with second order. A similar Taylor expansion about $x = 1$ shows second order convergence of $x_n \rightarrow 1$ when $\varphi^{-1} < x < 1$.